Numerical study of electrohydrodynamic atomization considering liquid wetting and corona discharge effects

Luan Ngoc Mai ✉ 🅾 ; Trung Hieu Vu ✉ 🅾 ; Thien Xuan Dinh 🅾 ; Hoai Duc Vu 🅾 ; Canh-Dung Tran 🅾 ;
Van Thanh Dau 🅾 ; Hieu Khanh Ngo 🅾

Check for updates

CrossMark

View
Online

Export
Citation

Numerical study of electrohydrodynamic atomization considering liquid wetting and corona discharge effects

View Online   Export Citation   CrossMark

Luan Ngoc Mai,[1,2,a] (iD) Trung Hieu Vu,[3,a] (iD) Thien Xuan Dinh,[4] (iD) Hoai Duc Vu,[3] (iD) Canh-Dung Tran,[5] (iD) Van Thanh Dau,[3] (iD) and Hieu Khanh Ngo[1,2,6] (iD)

AFFILIATIONS

[1]Department of Aerospace Engineering, Ho Chi Minh City University of Technology (HCMUT), 268 Ly Thuong Kiet Street, District 10, Ho Chi Minh City, Vietnam

[2]Vietnam National University Ho Chi Minh City, Linh Trung Ward, Thu Duc City, Ho Chi Minh City, Vietnam

[3]School of Engineering and Built Environment, Griffith University, Queensland, Australia

[4]Explosion Research Institute Inc., R&D Division, Tokyo, Japan

[5]School of Mechanical and Electrical Engineering, University of Southern Queensland, Queensland 4350, Australia

[6]VNU-HCM Key Lab. for Internal Combustion Engine, Ho Chi Minh City University of Technology (HCMUT), 268 Ly Thuong Kiet Street, District 10, Ho Chi Minh City, Vietnam

[a]Authors to whom correspondence should be addressed: mnluan.sdh212@hcmut.edu.vn and trunghieu.vu@griffithuni.edu.au

ABSTRACT

In this paper, the behavior of the cone-jet mode of fluid by electrohydrodynamic atomization (electrospray) is numerically simulated and investigated with the effect of liquid wetting and corona discharge effects. The simulation was performed with contact angle condition to fit the Taylor cone shape by experiments. Experimental data are provided to verify and validate the numerical method, followed by additional analyses on the effects of electrical conductivity, surface tension, flow rate, and fluid viscosity on the electrospray characteristics, including spray current and jet diameter. Numerical results by simulations are in reasonable agreement with experiments and consistent with the literature. Analyses on different contact angles suggest potentially major impacts of this factor on the cone-jet mode in high voltage and low flow rate circumstances. Furthermore, the influence of corona discharge on electrospray is also investigated by both electrospray–corona simulation and experiment using a high-speed camera, yielding a significant improvement in the numerical prediction for Taylor cone formation. Numerical results indicate that liquid wetting on capillary nozzles would be a vital factor for the Taylor cone formation in numerical electrospray–corona discharge studies.

NOMENCLATURE
Regular letters

A	Area of the discharge surface, m^2
Ca_e	Dimensionless electric capillary number
d_j	Jet diameter, m
$\boldsymbol{E}$	Electric field, $-\nabla\phi$
E_∞	Electric field intensity, V/m
E_{on}	Onset electric field
E_z	Electric field component in the perpendicular direction to the outlet, V/m
f_e	Electrostatic force, N/m^3

f_σ	Surface tension force, N/m^3
$\boldsymbol{g}$	Gravitational acceleration, m/s^2
I_d	Discharge current, A
$i.d$	Inner diameter, mm
I_{cond}	Conductive current, A
I_{conv}	Convective current, A
$i.d_r$	Ring inner diameter, mm
J	Current density, A/m^2
$\boldsymbol{n}_0$	Uncorrected interface normal vector
$\boldsymbol{n}_c$	Corrected interface normal vector
$\boldsymbol{n}_w$	Boundary wall normal vector
$o.d$	Outer diameter, mm

p	Pressure, Pa
Q	Liquid low rate, ml/h
r_E	Interelectrode distance, mm
d_{fil}	Nozzle sharp edges fillet diameter, mm
S	Outlet area, m^2
t	Time, s
$\boldsymbol{u}$	Fluid velocity, m/s
$\boldsymbol{u}_r$	Artificial compression term
U_z	Liquid velocity component in the perpendicular direction to the outlet, m/s
l_c	Cone length, mm
v_i	Ionic wind velocity, m/s
t_j	Time to first jet induction, s

Greek letters

γ_{liq}	Phase fraction of liquid
ε	Permittivity, F/m
ε_0	Permittivity of free space
ε_r	Dielectric constant
θ	Contact angle
θ_0	Angle between the uncorrected interface normal vector and the wall's normal vector
κ	Mean curvature of the free surface, m^{-1}
κ_e	Electrical conductivity of the fluid, S/m
μ	Fluid viscosity, Pa.s
μ_e	Mobility of charge of the gas
ρ	Fluid density, kg/m^3
ρ_c	Corona volumetric charge, C/m^3
ρ_e	Volumetric charge density, C/m^3
σ	Surface tension, N.m
ϕ	Electric potential, V
φ_c	Cone angle
θ_a	Actual contact angle between the liquid's interface and the nozzle's wall

Abbreviations

AC	Alternating current
CF	Carbon fiber
CSF	Continuum surface force
EHDA	Electrohydrodynamic atomization
N1	Nozzle 1
N2	Nozzle 2
VOF	Volume of fluid

Subscripts

e	Experiment
s	Simulation

I. INTRODUCTION

Electrohydrodynamic atomization (EHDA), also named as electrospray, refers to a process where a fluid jet is broken up into particles/fibers (droplets) by a high electric field. Owing to its potential, electrospray has been applied in various areas, including pharmaceutics,[1–4] food industry,[5,6] fuel spray and combustion,[7,8] electric propulsion,[9,10] and jet printing.[11,12] Among the working regimes of electrospray ionization, the single cone-jet mode in which only one jet is induced is the most used due to its stability, controllability, and high yield rate. This mode was first investigated by Taylor[13] who discussed the equilibrium condition of interfacial force with a specific semi-vertical angle (49.3°) of the conical shape, known as the Taylor cone. Notable early works include the publications of Rayleigh,[14] Zeleny,[15] and Taylor and Melcher[13,16] discussing fundamental aspects of electrospray. Taylor and Melcher[16] suggested a mathematical model, named as the leaky-dielectric, to explain the relationship of physical parameters involved and approximate the electric force exerted on the liquid surface. This work has been utilized in various studies to describe the formation and development of the Taylor cone into droplets.

Due to limits of the analytical approach, numerical methods have been used to study the formation and behavior of electrospray.[17] Several published works can be cited as follows: model the spraying of water and weak saline solutions at low-voltage using a double-layer nozzle;[18] approximate the characteristics of a novel carbon fiber emitter electrospray for mass spectrometric study;[19] and predict the electric potential in a large simulation domain.[20] Specifically, the numerical simulation of formation of the Taylor cone and its development into liquid jet and then droplets for various problems have attracted many researchers using different methods for different objectives. Herrada et al.[21] proposed a new interface tracking method, and Du and Chaudhuri[22] simulated the formation and breakup of droplets from axisymmetric charged liquid jets in electric fields. Several interesting physical phenomena occurring in charged droplet breakup and atomization, such as jet instability, necking, and the evolution of an unstable jet to droplet breakoff, were studied. Rahmanpour and Reza[23] and Panahi et al.[24] simulated the formation of the Taylor cone and into fluid jet under an external electric field[23] as well as the behavior of Newtonian viscoelastic jet.[24] Gamero-Castaño and Magnani[25] introduced numerical simulation employing Taylor's electric potential as a far-field boundary condition to achieve independence from geometry and potential of the electrodes, and the least-squared weighted residual method to the Young–Laplace equation for free surface tracking. Ouedraogo et al. found (i) the electrical properties of the liquid, such as electrical permittivity and conductivity can yield various mechanisms of fluid disintegration,[26] and (ii) the independence of the electrospray current on the applied voltage for conductive fluids.[27] Huh and Wirz[28] used a modified interpolation for electrical properties based on harmonic averages to improve the stability of the simulation of high conductivity fluids. Suo et al.[29] used a similar approach[28] to investigate the current transferred in the cone-jet mode for several different conductive liquids. These studies are most in good agreement with experimental results, strengthening the reliability of numerical simulations of the electrospray.

More interestingly, jet printing, one of the most common numerically investigated applications of electrospray, appears in numerous research works on various configurations, including conventional single nozzle[30–33] concentric non-conductive tip,[34] alternating current printer,[35] pulsating jet regime,[36,37] and coaxial nozzle.[38,39] All these works allow to study various physical behaviors of electrospray, which have enhanced the capability of electrospray in micro-/nano-manufacturing industry.

Previous studies concentrated on and validated the simulation of the Taylor cone by comparing its shape with experiment[18,20,23,28,29,39]

27 November 2023 07:46:51

or focused on the development of the Taylor cone into jet under different conditions to explore the physics of electrospray.[24,31,36–38] Experimental observations show that during electrospray, liquid tends to expand and cover the capillary nozzle's tip due to liquid wetting. However, so far numerical studies on the electrospray have either briefly mentioned or ignored the phenomenon, yielding inexact simulation of the cone shape and dimensions and inaccurate estimation of surface tension force based on the liquid's interface curvature and nozzle diameter. Furthermore, since corona discharge from nozzle electrode significantly affects the formation of the Taylor cone and the steady cone-jet mode, the introduction of corona discharge into simulations allows us to possibly approach real-life electrospray. Therefore, in this work, we perform electrospray simulations with a new approach in which the liquid wetting and corona discharge are additionally examined. The liquid wetting, considered as one of the key parameters, allows us to improve the simulating accuracy of the Taylor cone shape as well as its formulation and development. Meanwhile, electrospray–corona discharge integration is conducted to investigate the effects of corona discharge on electrospray and consolidate the importance of liquid wetting in electrospray analyses. The accuracy and reliability of the present simulation are investigated and evaluated by published works and, especially, experimental works using a high-speed camera to capture the formation and development of the Taylor cone.

II. EXPERIMENT APPARATUS

The numerical simulation for the jet formation at the nozzle tip is investigated and evaluated by experiment using the nozzle-to-ring configuration whose schema is described in Fig. 1. Liquid is fed to the tip of a nozzle, where its interface is deformed by an applied electric field before elongating into a jet. The system consists of a steel nozzle, a metal ring with an outer diameter of 10 mm and an inner diameter of 4.8 mm, a high-voltage power source, and a syringe pump. Two types of nozzles, Nozzle 1 (N1) and Nozzle 2 (N2), are employed for the experiment, with N1 featuring outer diameter (o.d) and inner diameter (i.d) of 0.3 and 0.15 mm, respectively, and N2 featuring o.d and i.d of 0.7 and 0.4 mm, respectively (stainless-steel G29 nozzle and G22 nozzle—Musashi Engineering, Inc., Japan). The distance between nozzle and ring (r_E) is adjusted at 4 mm for N1 and 7 mm for N2 to establish sufficient electric field. A high-speed camera (HHC X9 Pro, Mega Speed, USA) and a microscope camera (AM 4113, Dino-Lite,

Australia) are used to capture the formation of the Taylor cone and its development into fluid jet and droplets at the nozzle tip. The used liquid is polyethylene glycol with a molecular weight of 200 (PEG-200 - Merck, Australia).

The objective of this experiment is to observe the formation of Taylor cones, jet elongation, and propagation of liquid using both high-speed and microscope cameras. To achieve a stable Taylor cone and jet, the applied voltage is fixed at 3400 and 5400 V for N1 and N2, respectively. Meanwhile, a voltage of 5600 V is applied to capture the formation process of a Taylor cone with the high-speed camera. The flow rate is fixed at Q = 0.75 ml/h, which is determined by the approximation of the minimum flow rate required for a stable Taylor cone $Q \sim \sigma \varepsilon_r \varepsilon_0 / \rho \kappa_e$.[40] These experimental conditions allow for the observation and analysis of the physical phenomena of interest. Moreover, the contact angle of PEG-200 is determined by capturing the droplet on a stainless-steel plate with a digital camera (HHC X9 Pro, Mega Speed, USA). The measurements are performed using the ImageJ software (NIH). Here, similar material with metal nozzles is employed to reflect equivalent conditions with the liquid on nozzles.

III. SIMULATION MODEL
A. Governing equations
1. Fluidic field

This work employs the Taylor–Melcher's leaky-dielectric model[16] utilized in a great deal of electrospray research. This model provides a system of governing equations to consider the fluid-dynamic and electrostatic regimes involved in electrospray. For the fluid flow, the continuity and the momentum equations are

$$\frac{\partial \rho}{\partial t} + \nabla \cdot (\rho \boldsymbol{u}) = 0, \tag{1}$$

$$\rho \left[\frac{\partial \boldsymbol{u}}{\partial t} + (\boldsymbol{u} \cdot \nabla) \boldsymbol{u} \right] = -\nabla p + \mu \nabla^2 \boldsymbol{u} + \boldsymbol{f}_\sigma + \boldsymbol{f}_e + \rho \boldsymbol{g}, \tag{2}$$

where ρ is the fluid density, t is the time, $\boldsymbol{u}$ is the fluid velocity, p is the pressure, μ is the fluid viscosity, and $\boldsymbol{g}$ is the gravitational acceleration. Surface tension force $\boldsymbol{f}_\sigma$ and electrostatic force $\boldsymbol{f}_e$ are added to the system to consider multiphase behaviors and electrostatic involvement. In our approach by OpenFOAM, the surface tension force is calculated per unit volume by the continuum surface force (CSF) model,[41]

$$\boldsymbol{f}_\sigma = \sigma \kappa \nabla \gamma_{liq} = -\sigma \nabla \cdot \left(\frac{\nabla \gamma_{liq}}{|\nabla \gamma_{liq}|} \right) \nabla \gamma_{liq}, \tag{3}$$

where σ is the surface tension, κ is the mean curvature of the free surface, and the phase fraction of liquid γ_{liq} solved by the VOF method to capture the interface in the inhomogeneous fluid field[42] combined with a second convection term to increase the interface's resolution,

$$\frac{\partial \gamma_{liq}}{\partial t} + \nabla \cdot (\gamma_{liq} \boldsymbol{u}) + \nabla \cdot (\gamma_{liq} (1 - \gamma_{liq}) \boldsymbol{u_r}) = 0, \tag{4}$$

where $\boldsymbol{u_r}$ is an artificial compression term for higher interface resolution.[28]

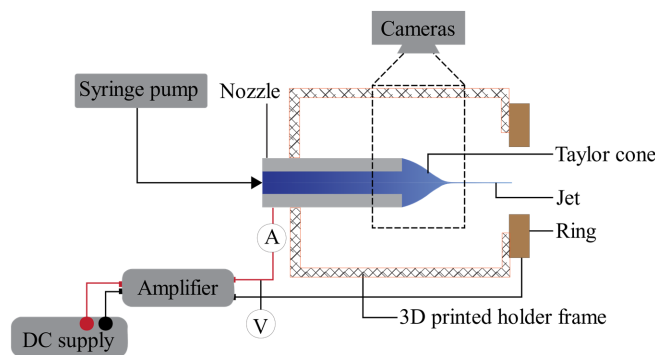Fluid density and viscosity are defined via arithmetic averaging with the phase fraction

FIG. 1. Schema of experiment installation (image of devices is in supplementary material S1).

$$\rho = \rho_1 \gamma_{liq} + \rho_2 (1 - \gamma_{liq}),$$
$$\mu = \mu_1 \gamma_{liq} + \mu_2 (1 - \gamma_{liq}). \quad (5)$$

Contact angle correction in OpenFOAM is implemented by some additional calculations in the process of estimating the interface curvature κ appearing in Eq. (3). These calculations modify the normal vector of the interface at the boundary wall in correspondence with the prescribed contact angle θ. The corrected interface normal vector $\boldsymbol{n}_c$ must be planar with both $\boldsymbol{n}_w$ and $\boldsymbol{n}_0$, arising the following:

$$\boldsymbol{n}_c = a\boldsymbol{n}_w + b\boldsymbol{n}_0, \quad (6)$$

where a and b are correction coefficients, $\boldsymbol{n}_w$ is the normal vector of the boundary wall, and $\boldsymbol{n}_0$ is the uncorrected interface normal vector. The coefficients a and b can be obtained by further considering $\cos\theta = \boldsymbol{n}_c.\boldsymbol{n}_w$, which guarantees that the angle between $\boldsymbol{n}_c$ and $\boldsymbol{n}_w$ equals the prescribed contact angle θ. Eventually, the below formulation can be derived from Eq. (6):

$$a = \frac{\cos\theta - \cos\theta_0 \cos(\theta_0 - \theta)}{1 - \cos\theta_0^2},$$
$$b = \frac{\cos(\theta_0 - \theta) - \cos\theta_0 \cos\theta}{1 - \cos\theta_0^2}, \quad (7)$$

where θ_0 is the angle between the uncorrected interface normal vector and the wall's normal vector ($\cos\theta_0 = \boldsymbol{n}_0.\boldsymbol{n}_w$). The corrected interface normal vector $\boldsymbol{n}_c$ is then normalized and used to derive the gradient of the phase fraction near the wall whose value is later considered in the VoF solver as suggested in Eq. (4). The detailed formulation of a and b can be found in supplementary material S2.1.

2. Electrostatic field

For the electrostatic regime, governing equations are solved iteratively with magnetic induction neglected to calculate the electrostatic force $\boldsymbol{f}_e$. The Gauss's law is first involved,

$$\nabla \cdot (\varepsilon \boldsymbol{E}) = \rho_e. \quad (8)$$

Integrating Eq. (8) with the relation $\boldsymbol{E} = -\nabla\phi$ formulates Poisson's equation for electrostatics,

$$\nabla^2(\phi) = \frac{-\rho_e}{\varepsilon}, \quad (9)$$

where ε is permittivity of the fluids ϕ and ρ_e are the electric potential and the volumetric charge density, respectively. Next, the conservation of charge equation is considered,

$$\frac{\partial \rho_e}{\partial t} + \nabla \cdot \boldsymbol{J} = 0, \quad (10)$$

where $\boldsymbol{J}$ is the current density, which can be expressed as Ohmic charge conduction and the charge convection in the fluid flow; thus, Eq. (10) can be rewritten as

$$\frac{\partial \rho_e}{\partial t} + \nabla \cdot (\rho_e \boldsymbol{u}) + \nabla \cdot (\kappa_e \boldsymbol{E}) = 0, \quad (11)$$

where κ_e is the electrical conductivity of the fluid. It is worth noting that the electrical conductivity and the electrical permittivity are defined by harmonic averages throughout the computational region,

which has been shown more reliable in EHD simulations than arithmetic averaging,[43]

$$\frac{1}{\varepsilon} = \frac{\gamma_{liq}}{\varepsilon_1} + \frac{1 - \gamma_{liq}}{\varepsilon_2},$$
$$\frac{1}{\kappa_e} = \frac{\gamma_{liq}}{\kappa_{e1}} + \frac{1 - \gamma_{liq}}{\kappa_{e2}}. \quad (12)$$

For incompressible fluids, electrostatic force is the summation of Coulombic force and polarization force due to the presence of interfacial charge and the inhomogeneity of the fluid field,[44]

$$\boldsymbol{f}_e = \rho_e E - \frac{1}{2} |\boldsymbol{E}|^2 \nabla\varepsilon. \quad (13)$$

3. Corona discharge

Additionally, as corona discharge is considered, its influence on the electric field must also be examined. In this study, we utilize a previously reported formulation.[45–53] First, Eq. (9) is modified into the following equation with ρ_c being the corona volumetric charge:

$$\nabla^2(\phi) = -\frac{(\rho_e + \rho_c)}{\varepsilon}. \quad (14)$$

Since the charge movement of the corona effect is purely in the gas phase of the field, i.e., there is no phase transition associated, the current density and the electrostatic force exerted are dictated by the following formulas:

$$J = \rho_c \boldsymbol{u} + \mu_e \rho_c \boldsymbol{E}, \quad (15)$$
$$\boldsymbol{f}_e = \rho_c \boldsymbol{E}, \quad (16)$$

where $\mu_e = 1.6 \times 10^{-4} \text{ m}^2/\text{V s}$ denotes the mobility of charge of the gas. Substituting Eq. (15) into Eq. (10) gains charge conservation equation for the corona discharge,

$$\frac{\partial \rho_c}{\partial t} + \nabla \cdot (\rho_c \boldsymbol{u}) + \nabla \cdot (\mu_e \rho_c \boldsymbol{E}) = 0. \quad (17)$$

As implied in Eqs. (16) and (17), the effects of electric field, which transport corona charge from its source to the reference electrode and exert Coulombic force on it, inducing ionic wind. Additionally, the boundary condition on the electrodes' discharge surface is set up by a density q_s as the function of discharge current I_d,

$$q_s = \frac{I_d}{\mu_e E_{\text{on}} A}, \quad (18)$$

where A is the area of the discharge surface and $E_{on} = 3.23 \times 10^6 \text{ V/m}$ is the onset electric field.[54]

B. Schema, mesh, and boundary conditions

We utilize the interFOAM solver of the open-source OpenFOAM package. This solver has been proven reliable in a wide range of complicated problems, such as cavitation or microfluidic capillary flows,[55] and, hence, emerges as the suitable solution for electrospray simulation. The additionally developed electrostatic solver and the existing fluid dynamic solver are coupled and solved
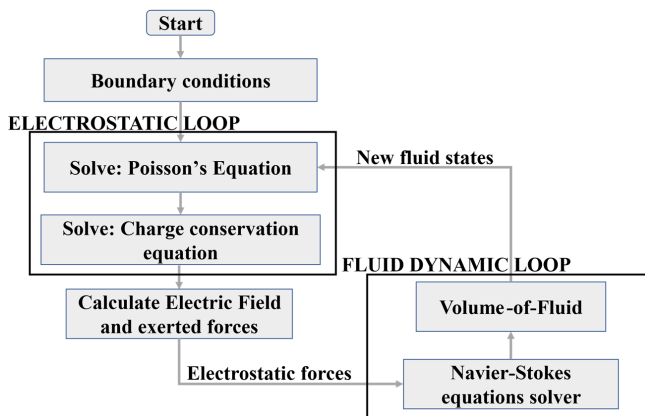
FIG. 2. Flowchart of the present numerical solver.

consecutively each time step. A detailed description of the solving procedure is presented in Fig. 2.

Simulations in this study involve two nozzle configurations, Nozzle 1 (N1) and Nozzle 2 (N2), whose sizes and conditions conform to experimental setups. Figure 3 shows the computational mesh and dimensional annotations of these configurations. The feeding nozzle (i) is positive electrode with constant voltage $\phi = \phi_0$. The ring electrode (ii − i.d$_r$ = 4.8 mm) is set with $\phi = 0$ V. The domain is enclosed by atmospheric boundaries with far-field conditions (more information of the computational model is in supplementary material S4.1 and S4.2). An axisymmetric 2D model is employed to simplify the
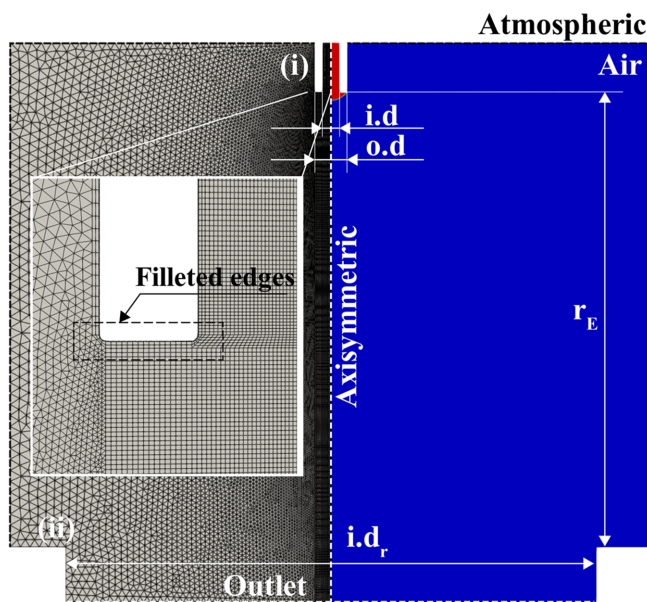

FIG. 3. The axisymmetric hybrid mesh model with (i) a feeding nozzle and (ii) a ring electrode. Inset figure shows a close-up view of the mesh resolution nearby the nozzle. The nozzle's sharp edges are filleted at $r_{fil} \approx 1.5\%o.d$ (see supplementary material S4.3 for detailed descriptions of the computational domains).

solution and reduce computational resources, with the front and back patches having a wedge condition with a 5° angle.

The computational mesh and domain, shown in Fig. 3, is constructed by the open-source *gMsh* mesh generator developed by Geuzaine and Remacle.[56] In this work, hybrid mesh resolution is employed to reduce the number of mesh elements whilst maintaining good flow alignment. The nozzle's sharp edges are filleted to guarantee better shape agreement with empirical nozzles as well as to describe somewhat more accurately the motion of the fluid on the surface of the capillary nozzle (see supplementary material S2.2). Here, total numbers of cells of 49 620 and 68 551 for N1 and N2 are obtained as minimum cell size is kept at 3 μm in both cases. For numerical schemes, we employ Gauss minmod for divergence components, Gauss linear corrected for Laplacian components, and cellLimited Gauss linear for gradient components. These schemes seem to provide good stability with an average time step of 3×10^{-7} s. Moreover, the physical properties of air and PEG-200 used in this work are shown in Table I.

The contact angle for nozzle is measured by experiment and used as the boundary condition for contact angle in simulations. Figure 4(a) shows (i) the experimental capture of a stationary PEG-200 droplet on a stainless-steel plate and (ii)(vi) verification simulation results of different contact angle conditions. Comparing each simulation case to experimental manifestation specifies most comparable shape between experiment and (iii) $\theta_s = 20°$. On top of that, measurement from the experimental capture also yields $\theta_e = 20°$, potentially indicating the reliability of the contact angle correction discussed in the previous section. Furthermore, the influence of the contact angle on the propagation mechanism of liquids is evaluated by fluid-dynamic (no electrostatic field) simulation results provided in Fig. 4(b). These results are obtained from completely similar boundary conditions, except for the contact angle, and at the same time instant. Case with no contact angle considered yields a liquid's surface being attached to the inner edge of the nozzle's tip, as commonly seen in preceding literature. Meanwhile, different contact angles result in a different wet tip's surface. Particularly, the smaller the liquid's contact angle is, the quicker its surface would propagate on the nozzle's wall and reach its outer edge. Therefore, to ensure adequate agreement with empirical state, the condition $\theta = 20°$ is applied on the nozzle boundary in subsequent electrospray simulations.

Corona discharge is considered as the inherent process of electrospray and may take various forms.[59] Discharge can initially originate from the metal electrode,[60] the tip of the cone where electric field intensity is high,[61] or molecular ions emission from jet/droplets breakup,[62,63] and can be measured in both dry-spray (no liquid flow rate) and wet-spray conditions.[59,64] Since the formulation process of

TABLE I. Physical properties of air and PEG-200.

Fluid	Air	PEG-200
Density ρ (kg/m^3)	1.225	1124
Dynamic viscosity μ (Pa s)	1.813×10^{-5}	0.06
Surface tension σ (N/m)	None	0.043
Dielectric constant ε_r	1	22 (Ref. 57)
Conductivity κ_e (mS/m)	1×10^{-9}	0.2 (Ref. 58)

(a)

(i) Experiment

20°

(ii) θ = 10°

Wall boundary

(iii) θ = 20°

(iv) θ = 40°

(v) θ = 60°

(vi) θ = 80°

(b)

(i) θ = 10°

(ii) θ = 20°

(iii) θ = 40°

(iv) θ = 60°
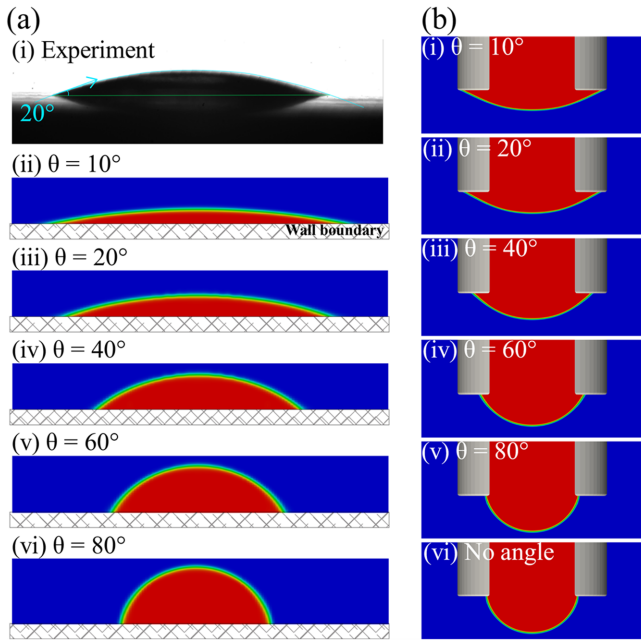
(v) θ = 80°

(vi) No angle

FIG. 4. (a) Experimental measurement of contact angle of PEG-200 on stainless steel plate and simulation of static droplet on wall boundary with different contact angle conditions. (b) Simulation shows different fluid propagation schemes due to different contact angles on nozzle; (vi) no angle represents zero-gradient condition $\partial \gamma_{liq}/\partial n = 0$. In both (a) and (b), the gravitational acceleration vector is downward.

the Taylor cone from a dry nozzle (no liquid on the nozzle's tip) is our concern here, we would assume that the corona discharge in our case solely originates from the outer sharp edge of the metal nozzle. The outer sharp edge is the closest point of the nozzle to the ring electrode, causing the electric field to be most intense at this position. Furthermore, the sharpness of the edge, despite filleted, can emphasize electric field intensity in the adjacent region. Given that corona discharge is a consequence of strong electric field and the feasibility of discharging from metal surface, we consider corona discharge from the outer edge of the nozzle in our analysis.

IV. RESULTS AND DISCUSSION

A. Simulation model validation

The empirical and numerical cone shapes for the two nozzle configurations are digitalized and plotted in Fig. 5. It is worth noting that in our simulation, the voltage in case N2 has to be $\phi_s = 6500$ V, approximately 20% higher than in experiment ($\phi_e = 5400$ V), to maintain steady cone-jet mode. It could be the 2D axisymmetric simplification of our model and the errors in experimental electrode arrangement that cause this difference. Nonetheless, our results show that the model that additionally considers liquid wetting and contact angle has produced visually comparable shapes with experiment in both cases. For the N1 configuration, experiment cone length (l_c) is at around 0.162 mm, while simulation registers a cone length of 0.142 mm (12% difference). This value for the N2 configuration is 0.45 and 0.41 mm for experiment and simulation, respectively, marking a 9% deviation. Simultaneously, the cone angles (φ_c) of the two sets of

data also show good agreement in both cases. For N1, cone angles are 82° in experiment and 91° in simulation, while in case N2, we obtain 84° and 94°, respectively. Moreover, empirical images showed that the jet produced in the N1 configuration is visibly thicker than in the N2 configuration, which can also be observed in simulation, indicating good qualitative agreement in terms of jet diameter between the results. Quantitatively, our measurement from the digitalized cones yields experimental jet diameter $d_{je} = 13.8\ \mu m$ and numerical jet diameter $d_{js} = 7.96\ \mu m$ for the N1 configuration, while these parameters are $d_{je} = 14.2$ and $d_{js} = 9.8\ \mu m$ for the N2 configuration. Overall, the inclusion of the contact angle and subsequent liquid propagation on the nozzle's wall accurately recreated the liquid state empirically manifested despite some deviations from experiment. Errors in voltage and measured quantities or inability of the model to produce the jet disintegration into a spray cloud as in experiments may be due to the axisymmetric model, grid resolution, and inaccuracy in image processing. These defects are to be addressed in future works. Considering the proposed scope of this study and the presented correlations between our experiments and simulations, the developed computational model can be deemed satisfactory and employed in next investigations.

B. Dimensionless analyses

The correlations between current and jet diameter with conductivity, voltage, surface tension, flow rate, and viscosity are widely discussed operational characteristics of electrospray. To optimize computing resources, we limit our simulations to employing solely the Nozzle 1 configuration, which enables us to investigate parametric relationships and confirm the dependability of our recently developed solver.

The total current of electrospray is the summation of convective current I_{conv} due to charge transport by the liquid flow and conductive current I_{cond} due to electrical conductivity and electric field.[19,28,33] In this work, total current is calculated by

$$I_{total} = I_{conv} + I_{cond} = \int_S (\rho_e U_z)dS + \frac{\pi(d_j)^2}{4}E_z\kappa_e, \qquad (19)$$

where U_z and E_z are liquid velocity and electric field component in the direction perpendicular to the outlet, S is the outlet's area, ρ_e and κ_e are as previously defined. Here, we integrate the value $\rho_e U_z$ on the whole outlet face to compute convective current and approximate the conductive current based on the jet diameter d_j whose estimation formulation can be found in supplementary material S3.

The correlation between spray current and jet diameter with electrical conductivity κ_e is graphed in Fig. 6. Simulations yields $I \propto \kappa_e^{0.22}$ and $d_j \propto \kappa_e^{-0.18}$ in the range 0.01 mS/m $\leq \kappa_e \leq$ 0.5 mS/m, which agrees well with early experimental reports by Tang and Kebarle[65] ($I \propto \kappa_e^{0.2-0.4}$) for $\kappa_e > 10^{-2}$ mS/m ($10^{-7}\ \Omega^{-1}$ cm^{-1}), and does not divert much from the asymptotic law by Gañán-Calvo[66] ($I \propto \kappa_e^{0.5}; d_j \propto \kappa_e^{-0.17}$). Qualitatively, this can be a consequence of the thicker charge concentration because of high conductivities, which exerts more Coulombic force under the influence of electric field and, subsequently, gives rise to higher jet velocities. The higher flow rate, coupled with the conservation of mass, leads to a reduction in the diameter of the jet, resulting in the commonly observed electrical
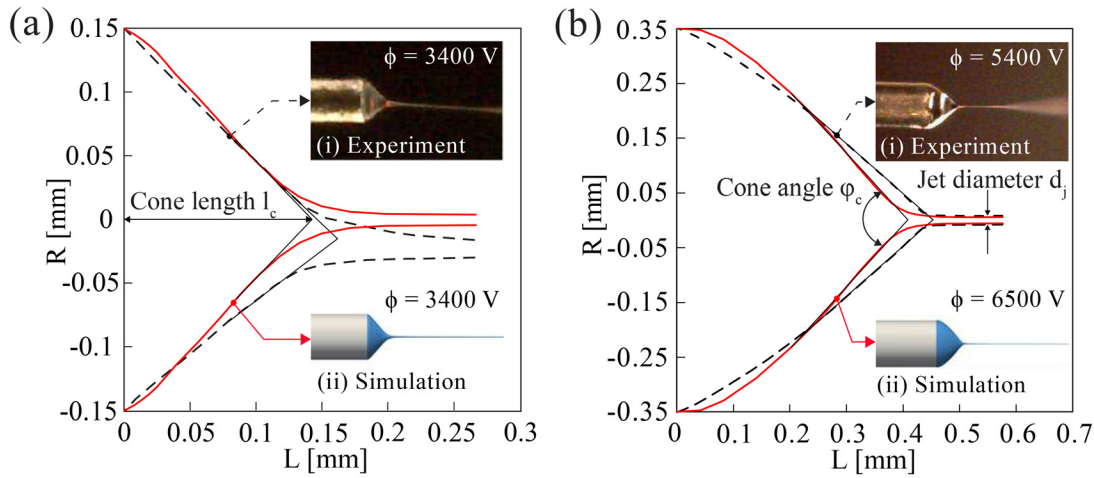
FIG. 5. Comparison between Taylor cone's shape of experiment (dashed line) and simulation (solid line) of (a) N1 nozzle configuration and (b) N2 nozzle configuration. Insets provide images of the (i) Taylor cone in experiment and (ii) 3D rendered phase fraction from simulation. Cone angle φ_c is approximated in the cone tip region represented by the black lines; cone length l_c is the distance from nozzle tip (L = 0 mm) to the intersection point of the black lines.

conductivity effects. (Additional simulation results are provided in supplementary material S4.3.)

Furthermore, the impacts of applied voltage and the liquid's surface tension are also comparable with other reports. Our model predicts an independence of current on the applied voltage and a reduction of jet diameter in the steady cone-jet range, as shown in Fig. 7(a). Here, simulations yield a constantly developing Taylor cone shape for lower voltage range ($\phi < 3400$ V) due to lack of equilibrium between feeding and spraying flow rate. We consider this range as unsteady cone-jet and neglect it in any dimensionless analyses. Under steady conditions, simulations have successfully reproduced the independent current–voltage relationship as has been reported in recently published experiment data.[67,68] The slight decrease in jet diameter with increasing applied voltage also shows good conformity with experimental gains of Gañán-Calvo *et al.*[69] While the jet diameter characteristic is caused by a growth in electrostatic force, the

FIG. 6. The variation of spray current and jet diameter with electrical conductivity.

voltage–current relation results from the compensation of the rise jet velocity for the contraction in diameter. As suggested by Eq. (19), an increase in velocity and a corresponding decrease in diameter would result in an unchanged current (see additional results in supplementary material S4.3). It is worth mentioning that our model also produces charge density ρ_e reliance with the phase fraction value γ_{liq}, which is used to calculate jet diameter; hence, both the conductive and convective currents are affected by jet diameter reduction. For the surface tension effects in the cone-jet mode, scaling law from[66] suggests analogous trends with conductivity ($I \propto \sigma^{0.5}; d_j \propto \sigma^{-0.17}$). As can be seen in Fig. 7(b), in the steadily working range, our model registers mildly consistent $I \propto \sigma^{0.34}$ for current, while jet diameter shows an agreed downward trend.

In Fig. 7, steady cone-jet can be achieved at higher voltage range and lower surface tension range. Additionally, in the unsteady cone-jet regions, the trend of current and diameter in the two graphs are almost opposite to each other. These features adhere to the relative variation of the electrostatic force and surface tension, which can be characterized by the dimensionless electric capillary number Ca_e,[70,71] represented in the following equation:

$$Ca_e = \frac{\varepsilon_r \varepsilon_0 E_\infty^2 D}{\sigma} \approx \frac{\varepsilon_r \varepsilon_0 \, \phi^2 D}{\sigma r_E^2}, \qquad (20)$$

where $\varepsilon_0 = 8.85 \times 10^{-12}$ F/m is the permittivity of free space, E_∞ is the electric field intensity, D is the outer diameter of the nozzle, σ is surface tension coefficient, ϕ is the applied voltage, and r_E is the inter-electrode distance. At this point, Figs. 7(a) and 7(b) can be plotted with the capillary number, obtaining Figs. 8(a) and 8(b). Our simulations produce steady cone-jet for $Ca_e \geq 1$ in both voltage and surface tension variation as electrostatic force further exceeds surface tension, whereas smaller capillary number $Ca_e < 1$ may result in dripping or spindle mode as sprayed and pumped flow rate cannot be equalized due to weaker electrostatic force.

The spray current and jet diameter variation with flow rate and viscosity are shown is Fig. 9. Our simulations predict a similar upward
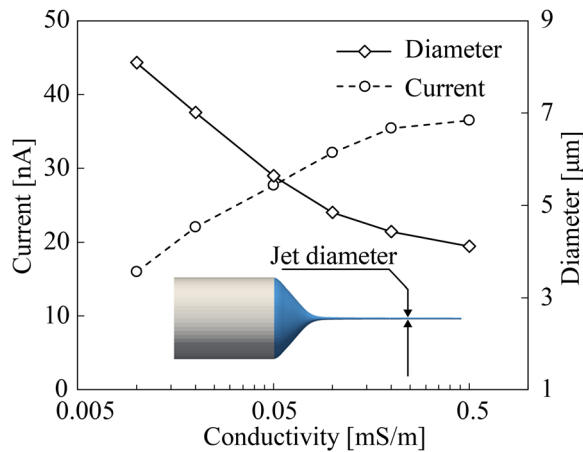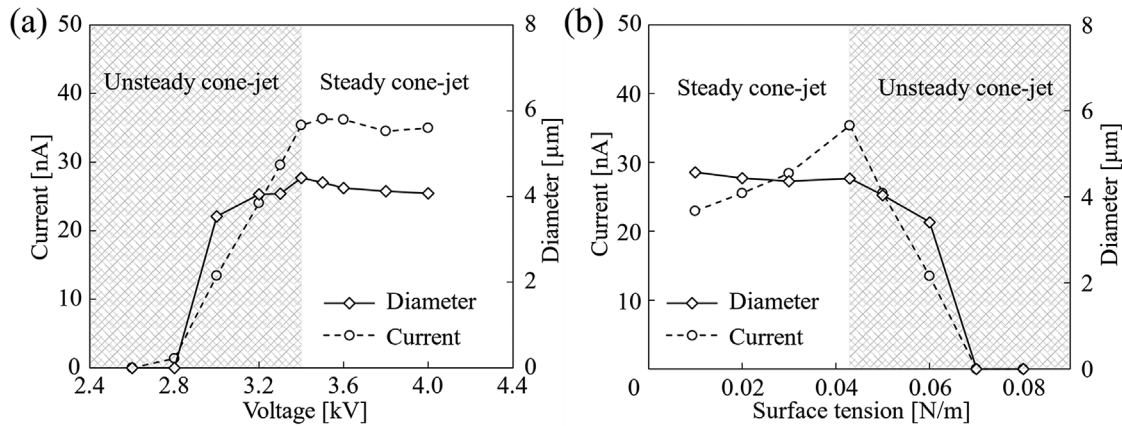
FIG. 7. Characteristics of electrospray: (a) spray current and jet diameter vs applied voltage and (b) spray current and jet diameter vs surface tension.

trend $I \propto Q^{0.92}$ and $d_j \propto Q^{0.2}$ in the steady cone-jet range, which agrees in order with scaling law[66] ($I \propto Q^{0.5}$; $d_j \propto Q^{0.5}$), yet overpredict the change in current and underestimate the increase in jet diameter. On the one hand, numerical results show negligible change in jet diameter as viscosity increases, which is comparable with reported work[72] predicting the insignificant effect of viscosity. Furthermore, scaling law from Gañán-Calvo[66] excludes viscosity on both spray current and jet diameter relations, implying the independence of these parameters on liquid's viscosity. On the other hand, our spray current results register an upward trend as viscosity value rises, which might have been mildly overestimated considering its insensitivity to viscosity.[66,73] This dissimilarity between simulations and empirical data on spray current was also obtained by Suo *et al.*[29] in which surface charge convection and strong tangential stress along the cone-jet surface were mentioned as the cause of the increasing trend of current. This explanation can also be applied in our study where we record a reduction of surficial charge density as viscosity increases due to the weakened recirculating motion (see supplementary material S4.3).

This motion arises due to the tangential electric stress along the Taylor cone's surface and is weakened or canceled when the liquid's viscosity is higher, which is consistent with experimental works of Barrero *et al.*[74,75]

C. Contact angle effects on a Taylor cone

To achieve better insight into the influence of contact angle on the cone-jet mode's characteristics, simulations on three contact angles conditions $\theta = 10°, 20°$, and $40°$ have been performed for both the N1 and N2 nozzle with $\phi = 3400$ V and $Q = 0.75$ ml/h. Figures 10(a) and 10(b) present Taylor cone's shape of N1 and N2 configuration, respectively, whereas Fig. 10(c) provides spray current and jet diameter variation with contact angles. Our results obtain negligible differences in the Taylor cone's shape despite considerable changes in liquid's contact angle, which results in the corresponding somewhat unaffected spray current and jet diameter characteristics. In both nozzles, our simulations produce relatively similar cone's shapes for all three contact angle conditions, except for slight differences at the
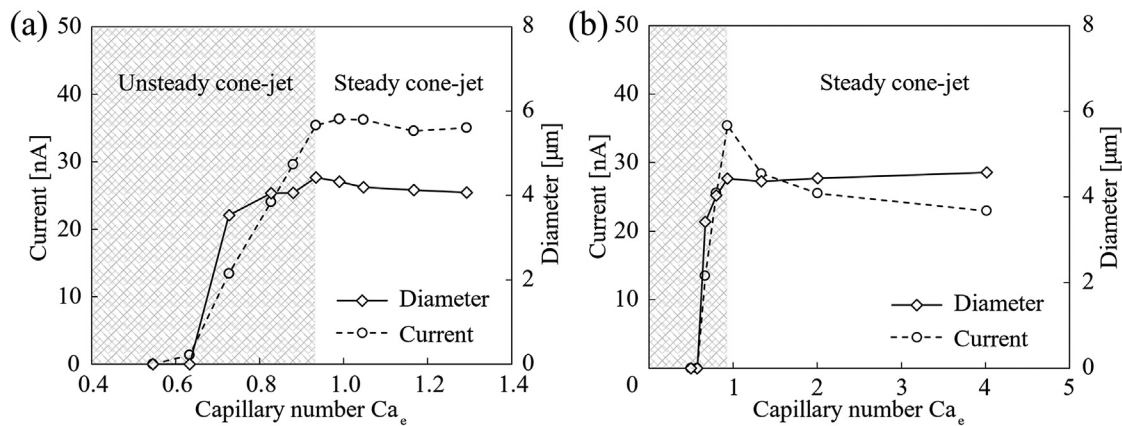

FIG. 8. Characteristics of electrospray: (a) spray current and jet diameter vs electric capillary number estimated from applied voltage ($\sigma = 0.048$ N/m); and (b) spray current and jet diameter vs electric capillary number estimated from the fluid surface tension ($\phi = 3400$ V).
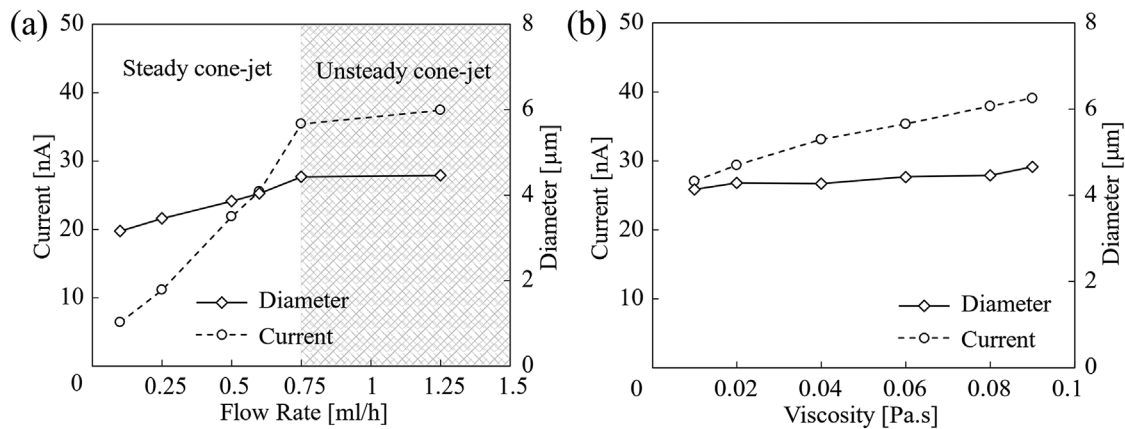
FIG. 9. Characteristics of electrospray: (a) spray current and jet diameter vs flow rate; and (b) spray current and jet diameter vs the fluid viscosity.

attachment positions at the filleted outer edge of the N1 setting [Fig. 10(a)]. However, this effect only localizes to liquid region adjacent to the nozzle's wall and does not affect the rest of the Taylor cone. Moreover, the actual angles between the liquid's surface and the wall of the nozzle's tip θ_a [annotated in Fig. 10(b)] are considerably higher than the contact angle conditions employed and even approaches $90°$ in some cases. Underlying reasons for these behaviors can be the overwhelming effects of other factors, namely applied voltage, flow rate, and other liquid's properties (conductivity, viscosity, and density)[76] on the cone's shape. For a chosen liquid, this potentially indicates that the roles of contact angle can be promoted under different voltage and flow rate. To avoid further complicating the investigation, we only conduct contact angle analyses under two separated conditions, one with a higher voltage ($\phi = 3600$ V; $Q = 0.75$ ml/h) and the other a lower flow rate ($Q = 0.6$ ml/h; $\phi = 3400$ V), using the N1 nozzle.

As observed in experiments,[77–80] higher applied voltage and lower flow rate can shorten the length of the Taylor cone l_c, enlarge the cone angle φ_c, and reduce the actual contact angle θ_a. Such behaviors of cone length and cone angle occur to balance the increasing electric stress due to rising voltage as well as the decreasing feeding volume due to lessening flow rate, which eventually keeps the cone-jet mode stabilized.[79]

Figure 10(d) shows spray current and jet diameter variation with contact angle for new voltage and flow rate condition while the cone's shape for each separated condition is provided in Figs. 10(e) and 10(f), respectively. One the one hand, in both voltage and flow rate conditions, no significant difference in spray current, and jet diameter as well as cone's shape is obtained between $\theta = 10°$ and $20°$. At these contact angles, our simulations produce noticeably shorter l_c, larger φ_c compared to cases in Figs. 10(a) and 10(b), conforming with the previously discussed experimental observations. Here, the actual contact angle θ_a is also smaller due to higher voltage and lower flow rate, yet still significantly larger than the declared contact angle of liquid ($\theta = 10°$, $20°$). On the other hand, in case $\theta = 40°$, the higher voltage and lower flow rate both yield receding cones with markedly higher spray currents and larger jet diameter [Fig. 10(d)]. At $\theta = 40°$, the surface tension induces force more inclined toward the center of the cone, whereas at $\theta = 10°$ and $20°$, this force is diverted more toward the

nozzle's wall. Therefore, instead of producing a shortened cone, the high contact angle $\theta = 40°$ develops a receding motion of the liquid's interface on the nozzle in which the liquid's surface quickly withdraws from the attachment position at the filleted outer edge, shrinking the Taylor cone radially. Despite not commonly reported, this retractive response can still be encountered in experiments.[81]

Overall, our results could imply that although the influence of other factors, such as voltage and flow rate, is more decisive in terms of modifying the Taylor cone's shape and the characteristics of the cone-jet mode, the liquid's contact angle is still impactful in certain circumstances, i.e., high applied voltages and low flow rates. The quantitative correlation between the receding mechanism with the liquid's contact angle θ as well as the actual contact angle θ_a remains an open problem and can be explored in dedicated research.

D. Corona discharge in electrospray

Figure 11 shows different liquid states at six consecutive time steps obtained from our experiments and simulations for the N2 configuration. Figure 11(a) includes numerical results neglecting any corona calculation, while Fig. 11(b) provides results considering corona discharge with a current of $I_d = 1$ μA. By further considering corona discharge, our simulations show better agreement with empirical captures displayed in Fig. 11(c). As stated, experimental data yield a slowly propagating liquid [at t_1 and t_2 in Fig. 11(c)] on the nozzle and the deformation of liquid's interface into steady cone-jet mode can only be obtained after the liquid completely covers the outer edge of the nozzle (t_3 and t_4). Similar behavior is reproduced by electrospray–corona simulation [Fig. 11(b)] where a cluster of analogously signed charge can be observed forming around the electrode (see Fig. 12), reducing the field intensity on the liquid surface to below its critical value for jet induction. As the nozzle edge is progressively covered by propagating liquid, the surface discharge is, therefore, obstructed and alleviated, causing an increase in electric field intensity. Due to this relationship, critical field value can be reached at t_4, gradually deforming the interface, and giving rise to jet afterward [at t_5 and t_6 in Figs. 11(b) and 11(c)]. On the other hand, if corona discharge is ignored, the field strength induces jet at very early time steps [t_2 to t_4,
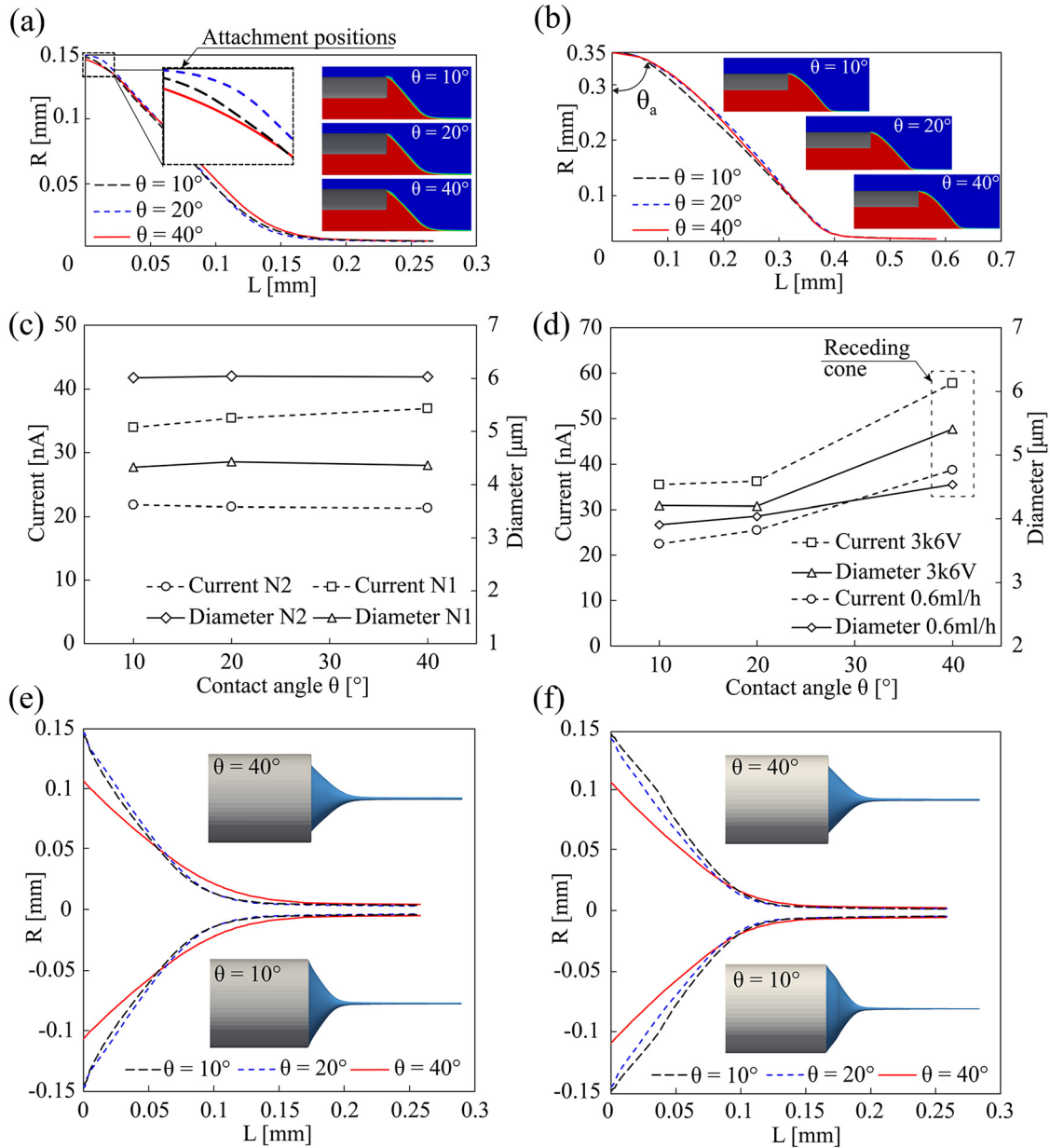
FIG. 10. Taylor cone shape under different contact angles for (a) N1 configuration; and (b) N2 configuration with the attachment positions and the actual angles between the liquid's surface and the wall of the nozzle's tip θ_a annotated; (c) spray current and jet diameter vs contact angle for N1 and N2 configuration under original $\phi = 3400\,V$ and $Q = 0.75\,ml/h$. (d) Spray current and jet diameter vs contact angle for N1 configuration with $\phi = 3600\,V$ and $Q = 0.6\,ml/h$; Taylor cone's shape variation with contact angle with (e) $\phi = 3600\,V$; and (f) $Q = 0.6\,ml/h$ for N1 configuration. Higher contact angle shrinks the Taylor cone radially at increased voltage and reduced flow rate, yielding receding Taylor cones.

Fig. 11(a)] when the liquid is still expanding on the nozzle, which is not consistent with empirical records.

In our simulations, we have shown that corona discharge has a delay effect to the formation of the cone-jet mode by weakening the electric field. Based on this, we reasonably predict that if the discharge is vigorous enough or originates from other positions on the nozzle (due to microscale surficial imperfections), steady cone-jet mode may not be achieved. Moreover, in cases where corona discharge and the cone-jet mode can coexist, further increase in applied voltage would not destabilize the cone-jet mode also because of the electric field reduction effect. These predictions are on par with many electrospray–corona research works,[59] indicating good physical conformity with empirical gains of our numerical model.
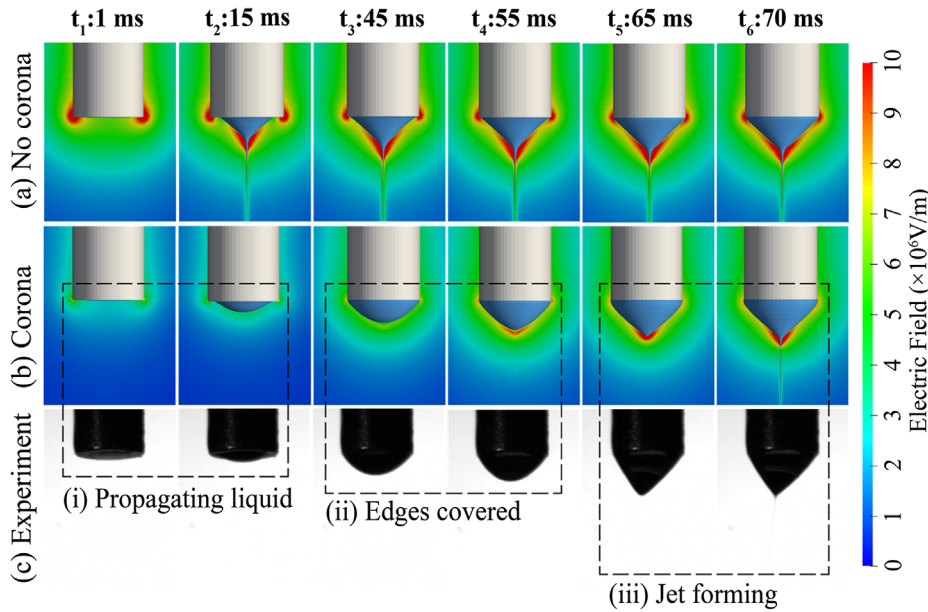
FIG. 11. High-frequency captured Taylor cone's shape at six consecutive time steps [t_1–t_6] from (a) simulation neglecting corona discharge; and (b) simulation involving corona discharge ($\phi = 6700$ V), and (c) experiment. Electric field intensity is rendered as background contour. Three stages of liquid progression annotated as follows: (i) propagating liquid—liquid is advancing from the inner edge to the outer edge of the nozzle; (ii) edges covered—liquid reached the outer edge and obstructs the corona discharge; (iii) jet forming—increased electric field is inducing jet at the tip of the Taylor cone.

Figure 12 provides additional results on the velocity field and the corona discharge contour at two greatly distinguished time instants. The discharge gives rise to a large cluster of charge (charge cloud) and an ionic wind field at t_2. Ionic wind is the movement of air caused by the momentum transferred from electrically charged molecules to neutral ones when they are accelerated by an electric field,[82] and it is the commonly known by-product of corona discharge. In this work,

the average velocity of the ionic wind measured at the outlet boundary stays at around $v_i = 2.6$ m/s for unobstructed discharge (t_2 in Fig. 12), which concurs in order with empirical measurements of pure corona-induced ionic wind of Zhang *et al.* (needle-to-ring: 1–8 m/s[83]) and Wang *et al.* (multiple-needles-to-mesh: 0.7–1.7 m/s[84] and two non-uniform needles-to-ring: 0.75–3.5 m/s[85]) or of our team's recently published works (dual pin discharge: 0–1.3 m/s).[47,49] At t_5, the
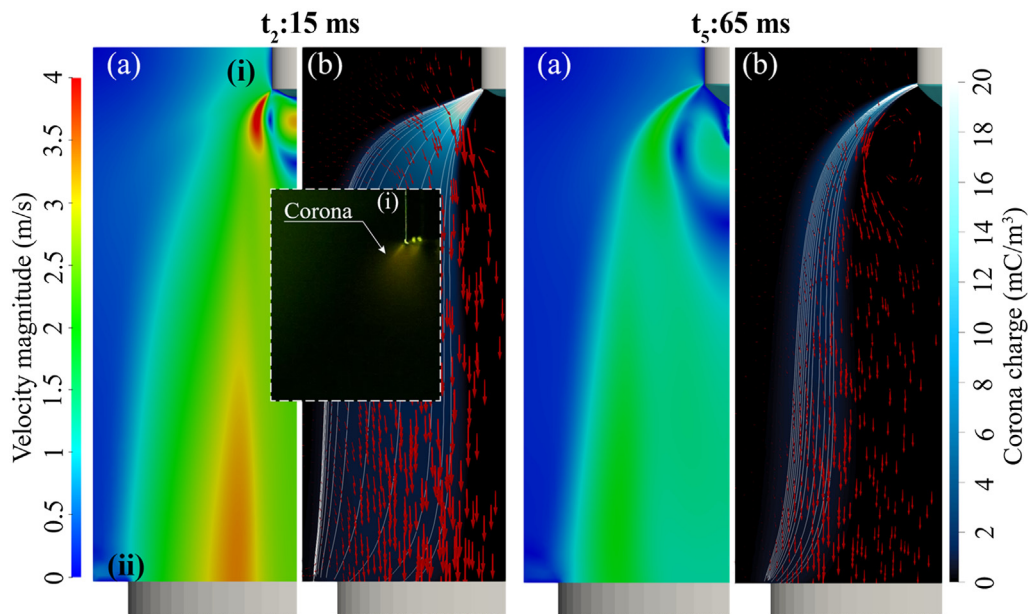

FIG. 12. Taylor cone's shape, ion wind velocity contour, and charge cloud from corona at t_2 and t_5. Background contours illustrate (a) ionic wind velocity and (b) charge density from corona; vector field represents an ionic wind field; and streamline denotes an electric field. Electrodes annotated, (i) nozzle and (ii) ring electrode. Inset shows a glowing region from nearby the outer edge of dry nozzle in high voltage, which is an indicator of strong electric field.
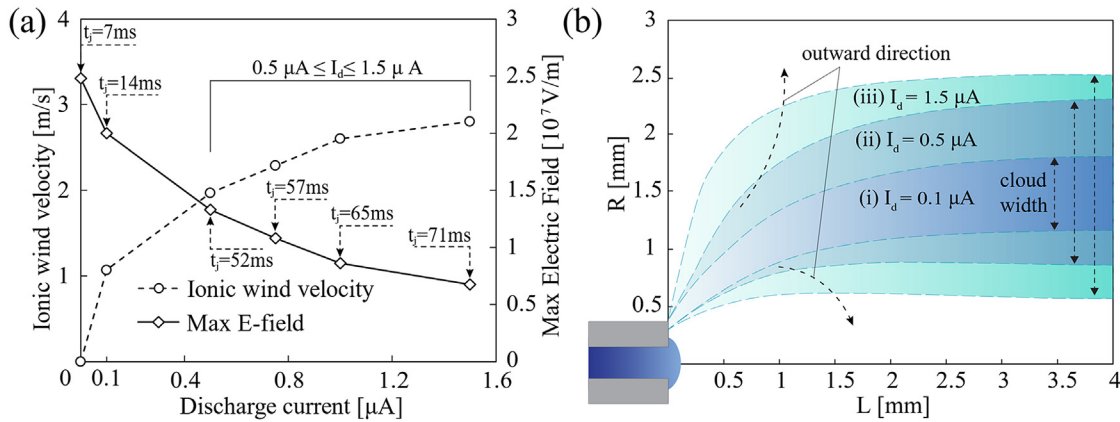
FIG 13. (a) Ionic wind velocity and maximum electric field intensity at the nozzle's tip variation with discharge current with time to first jet induction t_j annotated; and (b) the illustration of charge cloud from corona for different discharge currents. The boundary of the charge cloud is determined by a selected value of $\rho_c = 0.75 \, mC/m^3$ in all cases for comparative purpose.

discharge coverage and the velocity are significantly lessening, influencing the system in the manner described earlier. Additionally, the inset in Fig. 12 shows a long exposure capture of the corona discharge in the case of a dry nozzle, showing a glowing ionized region nearby and underneath the outer edge. This glow is the light emitted by excited neutral atoms when their electrons revert to ground state and can behave differently under different surrounding gaseous fields.[86] The characteristic glow indicates strong electric field, verifying the intense field in the vicinity of the relatively rounded edge in the contour results of Figs. 11(a) and 11(b) and confirming our earlier assumption regarding the origin of corona discharge in the electrospray.

The electrospray–corona simulation model developed in this study, with the proposed assumptions, is able to accurately reproduce the empirical formation of the Taylor cone and achieve reasonable consistency with existing literature regarding the effects and behaviors of corona discharge and ionic wind. The inclusion of corona discharge in the electrospray simulation highlights the crucial role of liquid wettability, which should be taken as a prominent impacting factor. Neglecting this factor may cause the solution flawed and unable to achieve a steady cone-jet mode.

Additionally, we perform multiple simulations with different discharge currents to further explore the effects of corona to the formulation of the Taylor cone. Figure 13(a) plots the ionic wind velocity and the maximum electric field (max E-field) at the nozzle's tip at $t_m = 30$ ms when the liquid has not yet reached the outer edge of the nozzle. Results for discharge-free case ($I_d = 0 \, \mu A$) are also included to provide a thorough comparative view. Simulations yield that both ionic wind velocity and max E-field follow a similar exponential relationship with discharge current, yet opposite in trend ($v_i \propto I_d^{0.34}$; $E_{max} \propto I_d^{-0.54}$). Simulated wind velocity is within 1–3 m/s, which still registers good order agreement with the discussed literature. In terms of electric field, simulations predict the field within 0.5×10^7 – 2×10^7 V/m, which is weakened from $E_{max} \approx 2.5 \times 10^7$ V/m in the discharge-free case. Here, we also calculate the time required for first jet induction t_j (elapsed time from the initial instance to the beginning of the induction of the first jet) to investigate the influence of discharge current on the delay effect of corona. At low current $I_d = 0.1 \, \mu A$, the weakened field can

still give rise to jet when the liquid is still propagating on the nozzle's surface, while in the range $0.5 \, \mu A \leq I_d \leq 1.5 \, \mu A$, the propagation of liquid and the delay effect can be clearly observed. In this range, the time t_j is relatively close with only several milliseconds difference (52; 57; 65; and 71 ms). This tendency suggests that higher discharge current requires a larger portion of the discharge area to be covered by liquid for electric field to sufficiently increase and exceed the critical value for jet induction.

Moreover, Fig. 13(b) provides a graph of cloud charge for three distinguished discharge currents, (i) $I_d = 0.1$, (ii) $I_d = 0.5$, and (iii) $I_d = 1.5 \, \mu A$ also at the same time step $t = 30$ ms. Broader cloud width is generated in cases of higher corona discharge current. As the discharge current increases, the Coulombic force in the charge cloud is more intense, expelling the charges outward, resulting in wider charge clouds (additional contour results in supplementary material S4.3).

In our study, the current values at which delay effect is observed ($0.5 \mu A \leq I_d \leq 1.5 \, \mu A$) are weak in intensity, yet realistically possible considering corona discharge current may vary from a few hundred nanoampere to a few dozen microampere for various configurations.[45,46,48,49,51,59] Moreover, the 2D axisymmetric model employed in this work may overemphasize the field reduction effect of the charge cloud from corona and the ionic wind velocity; thus, to avoid greater deviation from reality because of overprediction of these factors, low current range is investigated. Appropriate 3D models can be utilized in the future for more accurate numerical reproductions of corona discharge in electrospray.

V. CONCLUSION

A relevant numerical simulation for the cone-jet mode of electrospray has been carried out using a new approach in which the liquid wetting and corona discharge are considered as impacting parameters. Numerical results show that the present simulation achieves Taylor cone shapes very similar to those by experiments of two different configurations. Also, the electrospray's characteristics by the new approach, including the relations of the spray current and jet diameter with respect to the electrical conductivity, applied voltage, surface tension, flow rate, and viscosity are in reasonable agreement with those

27 November 2023 07:46:51

stated in published works.[65–69,72,73] The impacts of contact angles on the cone-jet mode are shown to be minor compared to those of applied voltage, flow rate, and other properties of liquids and, however, can be significant under higher voltages and lower flow rates. Furthermore, the electrospray–corona discharge integrated simulation, evidenced by experimental results, depicts that the introduction of corona discharge yields better and more appropriate simulation of the Taylor cone formation with higher accuracy compared with one by conventional non-corona simulations. The work demonstrates the crucial role of liquid wetting and corona discharge not only in the cone shape formation of the electrospray but also in further improving the numerical study of electrospray in the relation with corona discharge.

SUPPLEMENTARY MATERIAL

See the supplementary material for more information about the experiment installation, the contact angle correction formulation, additional experiment results, the computational model, jet diameter estimation, and more simulation results.

ACKNOWLEDGMENTS

AUTHOR DECLARATIONS
Conflict of Interest

The authors have no conflicts to disclose.

Author Contributions

Luan Ngoc Mai: Conceptualization (equal); Data curation (lead); Formal analysis (lead); Investigation (lead); Methodology (lead); Resources (lead); Software (lead); Visualization (lead); Writing – original draft (lead). **Trung-Hieu Vu:** Formal analysis (supporting); Investigation (supporting); Methodology (supporting); Visualization (supporting); Writing – original draft (supporting); Writing – review & editing (equal). **Thien Xuan Dinh:** Methodology (supporting); Software (supporting); Writing – review & editing (equal). **Hoai Duc Vu:** Formal analysis (supporting); Investigation (supporting); Methodology (supporting); Visualization (supporting); Writing – original draft (supporting); Writing – review & editing (equal). **Canh Dung Tran:** Conceptualization (equal); Data curation (supporting); Methodology (supporting); Supervision (equal); Writing – original draft (supporting); Writing – review & editing (equal). **Van Dau:** Conceptualization (equal); Data curation (supporting); Methodology (supporting); Supervision (equal); Writing – original draft (supporting); Writing – review & editing (lead). **Hieu Khanh Ngo:** Conceptualization (equal); Data curation (supporting); Methodology (supporting); Supervision (equal); Writing – review & editing (equal).

DATA AVAILABILITY

The data that support the findings of this study are available from the corresponding authors upon reasonable request.

REFERENCES

[1] A. O'Sullivan, B. Long, V. Verma, K. M. Ryan, and L. Padrela, "Solid-state and particle size control of pharmaceutical cocrystals using atomization-based techniques," Int. J. Pharm. **621**, 121798 (2022).

[2] M. S. Arshad, M. Mujeeb, S. Zafar, W. Q. Khan, M. Patel, B. Yousef, M.-W. Chang, E. Sayed, and Z. Ahmad, "EHDA engineering of Piroxicam-PVP components for pharmaceutical dosages," J. Drug Delivery Sci. Technol. **78**, 103927 (2022).

[3] V. T. Dau, T. T. Bui, C. D. Tran, T. V. Nguyen, T. K. Nguyen, T. Dinh, H. P. Phan, D. Wibowo, B. H. A. Rehm, H. T. Ta, N. T. Nguyen, and D. V. Dao, "In-air particle generation by on-chip electrohydrodynamics," Lab Chip **21**(9), 1779 (2021).

[4] A. Ali, A. Zaman, E. Sayed, D. Evans, S. Morgan, C. Samwell, J. Hall, M. S. Arshad, N. Singh, O. Qutachi, M.-W. Chang, and Z. Ahmad, "Electrohydrodynamic atomisation driven design and engineering of opportunistic particulate systems for applications in drug delivery, therapeutics and pharmaceutics," Adv. Drug Delivery Rev. **176**, 113788 (2021).

[5] Y. Man, C. Zhou, B. Adhikari, Y. Wang, T. Xu, and B. Wang, "High voltage electrohydrodynamic atomization of bovine lactoferrin and its encapsulation behaviors in sodium alginate," J. Food Eng. **317**, 110842 (2022).

[6] T. Anukiruthika, J. A. Moses, and C. Anandharamakrishnan, "Electrohydrodynamic drying of foods: Principle, applications, and prospects," J. Food Eng. **295**, 110449 (2021).

[7] D. Fredrich, E. Weiand, and A. Giusti, "Electrostatic fields for the control of evaporating charged fuel sprays," Int. J. Multiphase Flow **160**, 104312 (2023).

[8] T. Ahmed, A. Kourmatzis, G. Singh, and A. R. Masri, "Turbulent spray flames of kerosene issuing from a hybrid electrohydrodynamic-air-blast atomiser," Combust. Flame **239**, 111573 (2022).

[9] S. Maharaj, M. Yunus Malik, O. Allegre, and K. Lucy Smith, "Computationally examining the effect of plate thickness on hole-emitter-type electrospray thrusters," J. Propul. Power **39**, 331 (2023).

[10] J. Zhang, G. Cai, A. Shahzad, X. Liu, and W. Wang, "Ionic liquid electrospray behavior in a hybrid emitter electrospray thruster," Int. J. Heat Mass Transfer **175**, 121369 (2021).

[11] J. U. Park, M. Hardy, S. J. Kang, K. Barton, K. Adair, D. K. Mukhopadhyay, C. Y. Lee, M. S. Strano, A. G. Alleyne, J. G. Georgiadis, P. M. Ferreira, and J. A. Rogers, "High-resolution electrohydrodynamic jet printing," Nat. Mater. **6**, 782–789 (2007).

[12] N. Farjam, I. A. Spiegel, and K. Barton, "High-fidelity modeling and validation of electrohydrodynamic jet printing," Materialia **26**, 101578 (2022).

[13] G. I. Taylor, "Disintegration of water drops in an electric field," Proc. R. Soc. London A **280**, 383–397 (1964).

[14] L. Rayleigh, "XX. On the equilibrium of liquid conducting masses charged with electricity," London, Edinburgh Dublin Philos. Mag. J. Sci. **14**(87), 184–186 (1882).

[15] J. Zeleny, "Instability of electrified liquid surfaces," Phys. Rev. **10**(1), 1–6 (1917).

[16] J. R. Melcher and G. I. Taylor, "Electrohydrodynamics: A review of the role of interfacial shear stresses," Annu. Rev. Fluid Mech. **1**, 111 (1969).

[17] O. Lastow and W. Balachandran, "Numerical simulation of electrohydrodynamic (EHD) atomization," J. Electrostatics **64**(12), 850 (2006).

[18] O. Lastow and W. Balachandran, "Novel low voltage EHD spray nozzle for atomization of water in the cone jet mode," J. Electrostatics **65**(8), 490 (2007).

[19] A. K. Sen, J. Darabi, D. R. Knapp, and J. Liu, "Modeling and characterization of a carbon fiber emitter for electrospray ionization," J. Micromech. Microeng. **16**, 620 (2006).

[20] L. K. Lim, J. Hua, C.-H. Wang, and K. A. Smith, "Numerical simulation of cone-jet formation in electrohydrodynamic atomization," AIChE J. **57**(1), 57 (2011).

[21] M. A. Herrada, J. M. López-Herrera, A. M. Gañán-Calvo, E. J. Vega, J. M. Montanero, and S. Popinet, "Numerical simulation of electrospray in the cone-jet mode," Phys. Rev. E **86**(2), 026305 (2012).

[22] W. Du and S. Chaudhuri, "A multiphysics model for charged liquid droplet breakup in electric fields," Int. J. Multiphase Flow **90**, 46 (2017).

[23] M. Rahmanpour and R. Ebrahimi, "Numerical simulation of electrohydrodynamic spray with stable Taylor cone–jet," Heat Mass Transfer **52**(8), 1595 (2016).

[24] A. Panahi, A. R. Pishevar, and M. R. Tavakoli, "Numerical simulation of jet mode in electrospraying of Newtonian and viscoelastic fluids," Int. J. Multiphase Flow **129**, 103302 (2020).

[25] M. Gamero-Castaño and M. Magnani, "Numerical simulation of electrospraying in the cone-jet mode," J. Fluid Mech. **859**, 247 (2019).

[26] Y. Ouedraogo, E. Gjonaj, T. Weiland, H. D. Gersem, C. Steinhausen, G. Lamanna, B. Weigand, A. Preusche, A. Dreizler, and M. Schremb, "Electrohydrodynamic simulation of electrically controlled droplet generation," Int. J. Heat Fluid Flow **64**, 120 (2017).

[27] Y. Ouedraogo, E. Gjonaj, H. D. Gersem, and S. Schöps, "Simulation of transient electrospray dynamics in conductive fluids," IEEE Trans. Magn. **56**(3), 7511604 (2020).

[28] H. Huh and R. E. Wirz, "Simulation of electrospray emission processes for low to moderate conductivity liquids," Phys. Fluids **34**(11), 112017 (2022).

[29] X. Suo, K. Zhang, X. Huang, D. Wang, H. Jia, F. Yang, W. Zhang, J. Li, L. Tu, and P. Song, "Electrospray beam currents in the cone-jet mode based on numerical simulation," Phys. Fluids **35**(1), 013603 (2023).

[30] K. Mohammadi, M. R. Movahhedy, and S. Khodaygan, "A multiphysics model for analysis of droplet formation in electrohydrodynamic 3D printing process," J. Aerosol Sci. **135**, 72 (2019).

[31] L. Jiang, L. Yu, P. Premaratne, Z. Zhang, and H. Qin, "CFD-based numerical modeling to predict the dimensions of printed droplets in electrohydrodynamic inkjet printing," J. Manuf. Processes **66**, 125 (2021).

[32] D. Wang, Z. Abbas, Z. Du, Z. Du, L. Lu, K. Zhao, X. Zhao, Y. Yuan, H. Zong, Y. Cui, L. Suo, and J. Liang, "Phase field simulation of electrohydrodynamic jet droplets and printing microstructures on insulating substrates," Microelectron. Eng. **261**, 111817 (2022).

[33] S. K. Singh and A. Subramanian, "Phase-field simulations of electrohydrodynamic jetting for printing nano-to-microscopic constructs," RSC Adv. **10**, 25022 (2020).

[34] S.-Y. Kim, Y. Kim, J. Park, and J. Hwang, "Design and evaluation of single nozzle with a non-conductive tip for reducing applied voltage and pattern width in electrohydrodynamic jet printing (EHDP)," J. Micromech. Microeng. **20**(5), 055009 (2010).

[35] Z. Abbas, D. Wang, Z. Du, K. Zhao, Z. Du, L. Lu, Y. Cui, and J. Liang, "Numerical simulation of stable electrohydrodynamic cone-jet formation and printing on flexible substrate," Microelectron. Eng. **237**, 111496 (2021).

[36] Y. Guan, S. Wu, M. Wang, Y. Tian, C. Yu, W. Lai, and Y. Huang, "Numerical investigation of high-frequency pulsating electrohydrodynamic jet at low electric Bond numbers," Phys. Fluids **34**(1), 012001 (2022).

[37] Y. Guan, S. Wu, M. Wang, Y. Tian, W. Lai, and Y. Huang, "Numerical analysis of electrohydrodynamic jet printing under constant and step change of electric voltages," Phys. Fluids **34**(6), 062005 (2022).

[38] X. Zhao, D. Wang, Y. Lin, Y. Sun, T. Ren, J. Liang, and M. Madou, "Numerical simulation of coaxial electrohydrodynamic jet and printing nanoscale structures," Microsyst. Technol. **25**(12), 4651 (2019).

[39] D. Wang, Z. Abbas, L. Lu, X. Zhao, P. Xu, K. Zhao, P. Yin, and J. Liang, "Numerical modeling and analysis of coaxial electrohydrodynamic jet printing," Sci. Rep. **12**(1), 1924 (2022).

[40] C.-H. Chen, in *Electrokinetics and Electrohydrodynamics in Microsystems*, edited by A. Ramos (Springer, Vienna, 2011), p. 177.

[41] J. U. Brackbill, D. B. Kothe, and C. Zemach, "A continuum method for modeling surface tension," J. Comput. Phys. **100**(2), 335 (1992).

[42] C. W. Hirt and B. D. Nichols, "Volume of fluid (VOF) method for the dynamics of free boundaries," J. Comput. Phys. **39**(1), 201 (1981).

[43] G. Tomar, D. Gerlach, G. Biswas, N. Alleborn, A. Sharma, F. Durst, S. W. J. Welch, and A. Delgado, "Two-phase electrohydrodynamic simulations using a volume-of-fluid approach," J. Comput. Phys. **227**(2), 1267 (2007).

[44] J. R. Melcher, *Continuum Electromechanics/James R. Melcher* (MIT Press, Cambridge, Massachusetts, 1981).

[45] K. Adamiak and P. Atten, "Simulation of corona discharge in point–plane configuration," J. Electrost. **61**(2), 85 (2004).

[46] L. Zhao and K. Adamiak, "EHD flow in air produced by electric corona discharge in pin–plate configuration," J. Electrost. **63**(3), 337 (2005).

[47] V. T. Dau, T. X. Dinh, T. T. Bui, and T. Terebessy, "Bipolar corona assisted jet flow for fluidic application," Flow Meas. Instrum. **50**, 252 (2016).

[48] V. T. Dau, T. X. Dinh, T. Terebessy, and T. T. Bui, "Bipolar corona discharge based air flow generation with low net charge," Sens. Actuators, A **244**, 146 (2016).

[49] V. T. Dau, T. X. Dinh, T. T. Bui, C.-D. Tran, H. T. Phan, and T. Terebessy, "Corona based air-flow using parallel discharge electrodes," Exp. Therm. Fluid Sci. **79**, 52 (2016).

[50] V. T. Dau, T. X. Dinh, C.-D. Tran, T. Terebessy, and T. T. Bui, "Dual-pin electrohydrodynamic generator driven by alternating current," Exp. Therm. Fluid Sci. **97**, 290 (2018).

[51] T. X. Dinh, D. B. Lam, C.-D. Tran, T. T. Bui, P. H. Pham, and V. T. Dau, "Jet flow in a circulatory miniaturized system using ion wind," Mechatronics **47**, 126 (2017).

[52] N. T. Van, T. T. Bui, C. D. Tran, T. X. Dinh, H. P. Thanh, D. P. Van, T. C. Duc, and V. T. Dau, "Study on point-to-ring corona based gyroscope," in *IEEE 32nd International Conference on Micro Electro Mechanical Systems (MEMS)* (IEEE, 2019), p. 672.

[53] L. N. Mai, T. K. Nguyen, T. H. Vu, T. X. Dinh, C. D. Tran, H. P. Phan, T. Dinh, T. Nguyen, N. T. Nguyen, D. V. Dao, and V. T. Dau, "Development of boat model powered by electro-hydrodynamic propulsion system," in *IEEE 36th International Conference on Micro Electro Mechanical Systems (MEMS)* (IEEE, 2023), p. 1064.

[54] H. Toyota, S. Zama, Y. Akamine, S. Matsuoka, and K. Hidaka, "Gaseous electrical discharge characteristics in air and nitrogen at cryogenic temperature," IEEE Trans. Dielectr. Electr. Insul. **9**(6), 891 (2002).

[55] S. S. Deshpande, L. Anumolu, and M. F. Trujillo, "Evaluating the performance of the two-phase flow solver interFoam," Comput. Sci. Disc. **5**(1), 014016 (2012).

[56] C. Geuzaine and J.-F. Remacle, "Gmsh: A 3-D finite element mesh generator with built-in pre- and post-processing facilities," Int. J. Numer. Methods Eng. **79**(11), 1309 (2009).

[57] R. J. Sengwa, K. Kaur, and R. Chaudhary, "Dielectric properties of low molecular weight poly(ethylene glycol)s," Polym. Int. **49**(6), 599 (2000).

[58] M. Chereches, D. Bejan, E. I. Chereches, A. Alexandru, and A. A. Minea, "An experimental study on electrical conductivity of several oxide nanoparticle enhanced PEG 400 fluid," Int. J. Thermophys. **42**(7), 104 (2021).

[59] A. Jaworek, A. Sobczyk, T. Czech, and A. Krupa, "Corona discharge in electrospraying," J. Electrost. **72**(2), 166 (2014).

[60] B. Pongrác, H.-H. Kim, N. Negishi, and Z. Machala, "Influence of water conductivity on particular electrospray modes with dc corona discharge—Optical visualization approach," Eur. Phys. J. D **68**(8), 224 (2014).

[61] Y. Guo, S. Li, Z. Wu, K. Zhu, Y. Han, and N. Wang, "Interaction between electrospray using ionic liquid and simultaneous corona discharge under positive and negative polarity," Phys. Plasmas **26**(7), 073511 (2019).

[62] M. Gamero-Castaño and A. Cisquella-Serra, "Electrosprays of highly conducting liquids: A study of droplet and ion emission based on retarding potential and time-of-flight spectrometry," Phys. Rev. Fluids **6**(1), 013701 (2021).

[63] M. Gamero-Castaño and M. Galobardes-Esteban, "Electrospray propulsion: Modeling of the beams of droplets and ions of highly conducting propellants," J. Appl. Phys. **131**(1), 013307 (2022).

[64] S. Kim, M. Jung, S. Choi, J. Lee, J. Lim, and M. Kim, "Discharge current of water electrospray with electrical conductivity under high-voltage and high-flow-rate conditions," Exp. Therm. Fluid Sci. **118**, 110151 (2020).

[65] L. Tang and P. Kebarle, "Effect of the conductivity of the electrosprayed solution on the electrospray current. Factors determining analyte sensitivity in electrospray mass spectrometry," Anal. Chem. **63**(23), 2709 (1991).

[66] A. Gañán-Calvo, "On the general scaling theory for electrospraying," J. Fluid Mech. **507**, 203 (2004).

[67] Y. Gan, Z. Jiang, H. Li, Y. Luo, X. Chen, Y. Shi, Y. Yan, and Y. Yan, "A comparative study on droplet characteristics and specific charge of ethanol in two small-scale electrospray systems," Sci. Rep. **9**(1), 18791 (2019).

[68] J. Y. Kim, S. J. Lee, G. Y. Baik, and J. G. Hong, "Viscosity effect on the electrospray characteristics of droplet size and distribution," ACS Omega **6**(44), 29724 (2021).

[69] A. M. Gañán-Calvo, J. Dávila, and A. Barrero, "Current and droplet size in the electrospraying of liquids. Scaling laws," J. Aerosol Sci. **28**(2), 249 (1997).

[70]E. Castillo-Orozco, A. Kar, and R. Kumar, "Non-dimensional groups for electrospray modes of highly conductive and viscous nanoparticle suspensions," Sci. Rep. **10**(1), 4405 (2020).

[71]A. Yazdekhasti, A. Pishevar, and A. Valipouri, "Investigating the effect of electrical conductivity on electrospray modes," Exp. Therm. Fluid Sci. **100**, 328 (2019).

[72]J. Rosell-Llompart and J. Fernández de la Mora, "Generation of monodisperse droplets 0.3 to 4 μm in diameter from electrified cone-jets of highly conducting and viscous liquids," J. Aerosol Sci. **25**(6), 1093 (1994).

[73]J. F. De La Mora and I. G. Loscertales, "The current emitted by highly conducting Taylor cones," J. Fluid Mech. **260**, 155 (1994).

[74]A. Barrero, A. M. Gañán-Calvo, J. Dávila, A. Palacio, and E. Gómez-González, "Low and high Reynolds number flows inside Taylor cones," Phys. Rev. E **58**(6), 7309 (1998).

[75]A. Barrero, A. M. Gañán-Calvo, J. Dávila, A. Palacios, and E. Gómez-González, "The role of the electrical conductivity and viscosity on the motions inside Taylor cones," J. Electrost. **47**(1), 13 (1999).

[76]M. Cloupeau and B. Prunet-Foch, "Electrohydrodynamic spraying functioning modes: A critical review," J. Aerosol Sci. **25**(6), 1021 (1994).

[77]J. F. De La Mora, "The effect of charge emission from electrified liquid cones," J. Fluid Mech. **243**, 561 (1992).

[78]H. Park, K. Kim, and S. Kim, "Effects of a guard plate on the characteristics of an electrospray in the cone-jet mode," J. Aerosol Sci. **35**(11), 1295 (2004).

[79]Z. Wang, Q. Wang, B. Li, Y. Zhang, J. Wang, and J. Tu, "An experimental investigation on cone-jet mode in electrohydrodynamic (EHD) atomization," Exp. Therm. Fluid Sci. **114**, 110054 (2020).

[80]H. Zhou, Z. Shi, X. Wan, H. Fang, D.-G. Yu, X. Chen, and P. Liu, "The relationships between process parameters and polymeric nanofibers fabricated using a modified coaxial electrospinning," Nanomaterials **9**(6), 843 (2019).

[81]J. Zheng, K. Zhang, J. Jiang, X. Wang, W. Li, Y. Liu, J. Liu, and G. Zheng, "Jet behaviors and ejection mode recognition of electrohydrodynamic direct-write," AIP Adv. **8**(1), 015122 (2018).

[82]F. Plouraboué, "Flying with ionic wind," Nature **563**, 476 (2018).

[83]Y. Zhang, L. Liu, Y. Chen, and J. Ouyang, "Characteristics of ionic wind in needle-to-ring corona discharge," J. Electrost. **74**, 15 (2015).

[84]J. Wang, Y.-X. Cai, X.-H. Li, Y.-F. Shi, and Y.-C. Bao, "Electrically-induced ionic wind flow distribution and its application for LED cooling," Appl. Therm. Eng. **138**, 346 (2018).

[85]J. Wang, Y.-J. Liu, T. Zhu, Y.-Q. Chen, R.-J. Cai, and G.-K. Liu, "Flow distribution and cooling performance of needle-to-ring ionic wind blowers with multiple electrodes," Int. J. Heat Mass Transfer **193**, 122971 (2022).

[86]N. M. Uchizono, P. L. Wright, A. L. Collins, and R. E. Wirz, "Emission spectra of glows produced by ionic liquid ion sources," Appl. Phys. Lett. **121**(15), 154101 (2022).